Chapter 21
Superlubricity in Layered Nanostructures

Seymur Cahangirov and Salim Ciraci

Abstract Interaction between two surfaces in relative motion can give rise to energy dissipation and hence sliding friction. A significant portion of the energy is dissipated through the creation of non-equilibrium phonons. Recent advances in material synthesis have made the production of specific single layer honeycomb structures and their multilayer phases, such as graphene, graphane, fluorographene, MoS_2 and WO_2. When coated to the moving surfaces, the attractive interaction between these layers is normally very weak and becomes repulsive at large separation under loading force. Providing a rigorous quantum mechanical treatment for the 3D sliding motion under a constant loading force within Prandtl-Tomlinson model, we derive the critical stiffness required to avoid stick-slip motion. Also these nanostructures acquire low critical stiffness even under high loading force due to their charged surfaces repelling each other. The intrinsic stiffness of these materials exceeds critical stiffness and thereby the materials avoid stick-slip regime and attain nearly dissipationless continuous sliding. Remarkably, layered WO_2 a much better performance as compared to others and promises a potential superlubricant nanocoating. The absence of mechanical instabilities leading to conservative lateral forces is also confirmed directly by the simulations of sliding layers. Graphene coated metal surfaces also attain superlubricity and hence nearly frictionless sliding through a charge exchange mechanism with metal surface.

21.1 Introduction

Organisms in both micro and macro scales use friction to move. The way nature uses friction has frequently been an inspiration for scientific community. While the presence of friction is so important in our life, its absence is desperately demanded in

S. Cahangirov
Nano-Bio Spectroscopy Group, Departamento Fisica de Materiales, Centro de Fisica de Materiales CSIC-UPV/EHU-MPC and DIPC, Universidad Del Pais Vasco,
Av. Tolosa 72, 20018 San Sebastian, Spain
e-mail: seycah@gmail.com

S. Ciraci (✉)
Department of Physics, Bilkent University, 06800 Ankara, Turkey
e-mail: ciraci@fen.bilkent.edu.tr

E. Gnecco and E. Meyer (eds.), *Fundamentals of Friction and Wear on the Nanoscale*, NanoScience and Technology, DOI 10.1007/978-3-319-10560-4_21

most of our technological applications. We loose a substantial portion of the energy and material that we produce due to friction. Achieving superlubricity would help us to stop wasting enormous resources for nothing but producing heat of no use. Superlubricity can increase stability and sustainability of our technology alongside increasing its efficiency.

The key to achieve superlubricity is to understand friction in the most fundamental level. To this end, one expect that theoretical studies can help us to design superlubricant materials. Following this spirit, we organized this chapter starting with discussions of fundamental aspects of friction, building theoretical and computational methods to design materials and finally predicting novel materials that could be used as superlubricants. To achieve our objective we considered the exceptional properties of single layer honeycomb structures to exploit whether the surfaces in relative motion can attain superlubricity when coated with these single layer materials.

21.1.1 Dissipation Phenomena

Friction is not a fundamental physical force like gravity or electromagnetic interaction. It is a manifestation of a deeper phenomena called dissipation. Dissipation arises in systems having large number of interacting degrees of freedom. In sufficiently large systems, the macroscopic behavior of the system is generally irreversible even though the microscopic interactions are governed by reversible dynamics. In such systems, there is a probability distribution of states corresponding to equilibrium which occupies the largest volume in the configurational phase space. Any non-equilibrium distributions of states are less probable and eventually they are equilibrated through microscopic interactions.

In the case of friction, the dissipation of nonequilibrium phononic and electronic states have important role and it is governed by interactions among themselves and with each other. For example, phonons arise from the harmonic interaction between ions. However, the interaction between phonons themselves is governed by anharmonic terms of ionic interactions. In a perfectly harmonic crystal, non-equilibrium phononic states would remain in their initial distribution while in a highly anharmonic crystal they are quickly equilibrated through phononic dissipation.

21.1.2 Adiabatic Versus Sudden Processes

In sliding friction the non-equilibrium phononic and electronic states can be generated in two ways. The first way is generation through adiabatic processes. This kind of processes are generally not localized in space or time, which means that one can't show a microscopical region where such events start or end. For example, when two identical surfaces with weak interactions are sliding over each other

with equal but opposite center of mass velocities (which are well below the atomic vibration velocities), the system possesses an adiabatic non-equilibrium. The equilibrium configuration for such system is reached when atoms in both surfaces have same velocity distribution. The system will dissipate until this equilibrium is reached and all mechanical energy is transformed into random atomic vibrations. The surfaces will feel a force opposite and proportional to their center of mass velocity. This is, in general, the case for dissipative systems with adiabatic non-equilibrium generation mechanisms. The phononic and electronic dissipation mechanisms discussed above can be considered as examples in which the non-equilibrium state is generated adiabatically.

The second way is to generate non-equilibrium states through sudden processes. In this case, the process of generation can be traced by looking in a certain microscopical region in a certain time. As an example, consider a surface with asperities which have adhesive interaction with each other. When such surfaces are sliding over each other asperities that come close will cling to each other. Then they will be stretched due to the relative motion of surfaces that they are attached to. At some critical strain asperities will suddenly detach from each other and release all energy they have stored during the stretching as a burst of non-equilibrium phonons. Sliding systems which have this kind of microscopic events are said to be in the stick-slip regime.

Here it is important to point out that, if a non-equilibrium state is generated then it will be certainly dissipated no matter how weak the dissipation mechanisms are. The strength of the dissipation mechanisms only determine the time interval in which the equilibrium is reached. There is no way to regain the energy that comes off during the generation of non-equilibrium states. For this reason, the sudden processes determine the frictional properties of the systems which are in the stick-slip regime. In such systems the microscopic dissipation mechanisms have less importance and are usually lumped in a single coefficient as in (21.1).

21.1.3 Prandtl-Tomlinson Model

In the late 1920s when Einstein and Bohr were having a debate on philosophical issues brought by the newly developing quantum theory, Prandtl [1] and Tomlinson [2] separately developed concepts which are still at the heart of much older problem of friction. Their model explained the weak dependence of friction on sliding velocity. Here we present the important aspects of this model.

We start by pointing out that, Prandtl-Tomlinson model is one of the simplest yet being one of the most effective models describing the generation of non-equilibrium phonons. In this model, an elastic spring is dragged over a surface, as shown in Fig. 21.1a. The tip of this spring is interacting with the surface according to some potential energy landscape depending on the position of the tip on the surface. The other end of the spring (or the head of the spring) is pulled with constant velocity in certain direction. The restoring force on the tip is assumed to be directly proportional with the deviation of the tip from its equilibrium position. As mentioned in the

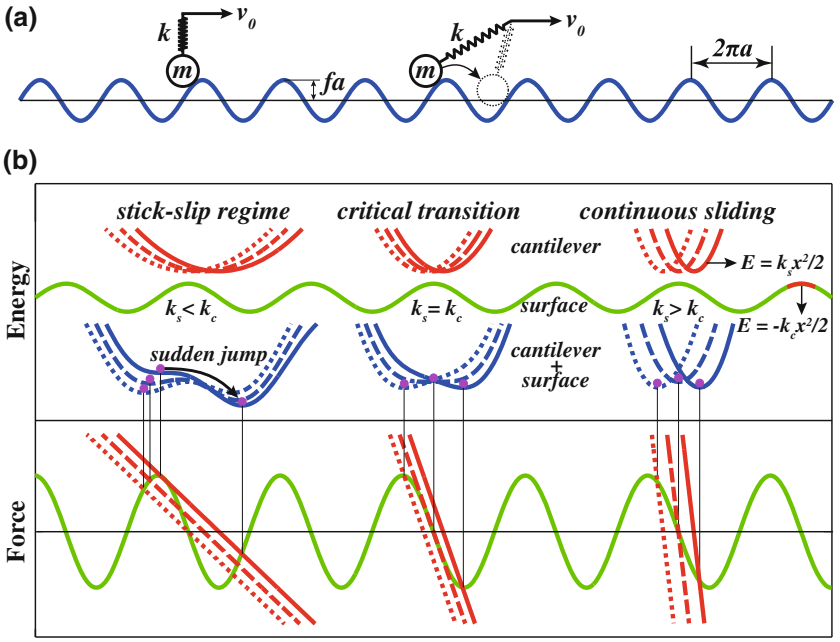

Fig. 21.1 **a** Prandt-Tomlinson model. **b** Schematic representation of stick-slip regime (*left*), critical transition (*middle*) and continuous sliding regime (*right*) in Prandtl-Tomlinson model. *Upper part* the potential energy curves of the surface (*green lines*) and of the tip (+cantilever) (*red lines*); *lower part* force variation of the surface (*green lines*) and of the tip (*red lines*). *Blue lines* represent the potential energy of the tip and surface. The *magenta dot* shows the position of the tip on the surface, while its other end is positioned at the minimum of the parabola shown with *red lines* in the *upper part*. The *dotted*, *dashed* and *solid lines* correspond to three different tip positions moving to the *right*

previous section, the dissipation due to interactions of the tip with surface atoms is lumped in a microscopic friction term proportional to the velocity of the tip. Assuming that the interaction between the tip and the surface has a sinusoidal profile one can write an equation of motion for the tip as following;

$$m\ddot{x} = -m\gamma\dot{x} + k(v_0 t - x) + f\sin(x/a) \tag{21.1}$$

which can be written in dimensionless form as;

$$\ddot{\tilde{x}} = \tilde{\gamma}\dot{\tilde{x}} + \tilde{k}(\tilde{v_0}\tilde{t} - \tilde{x}) + \sin(\tilde{x}) \tag{21.2}$$

where dimensionless variables are defined as $\tilde{x} = x/a$, $\tilde{\gamma} = \gamma\sqrt{ma/b}$, $\tilde{k} = ka/f$, $\tilde{v_0} = v_0\sqrt{m/ba}$ and $\tilde{t} = t\sqrt{b/ma}$. Here the most important parameter is $\tilde{k}$ which represents the ratio of the stiffness of the tip to the curvature of surface energy at its maximum points. If $\tilde{k} > 1$ the total energy of the tip-surface system always have one

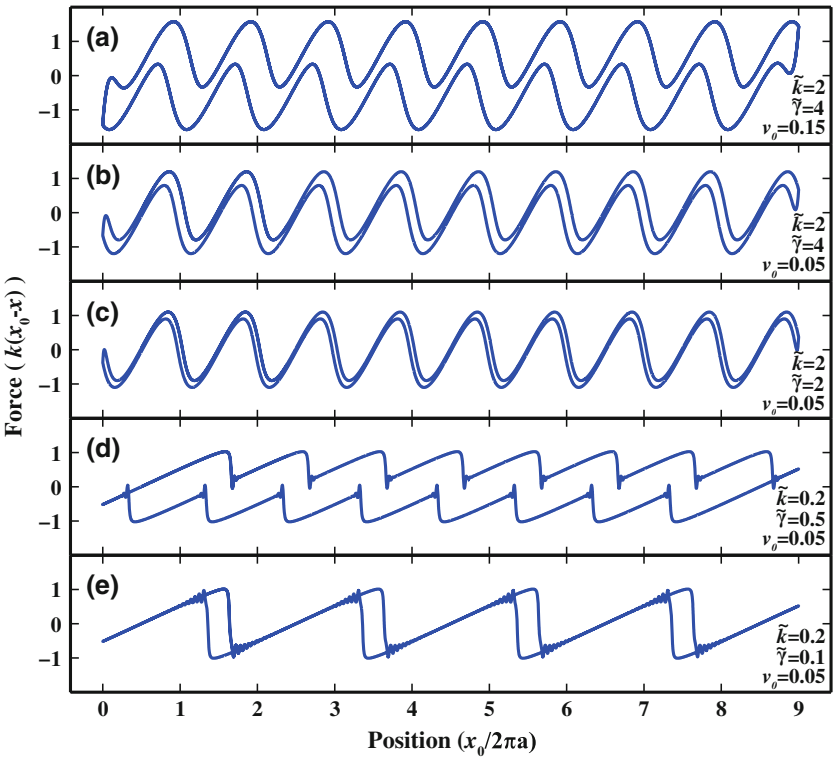

Fig. 21.2 Friction force felt by the tip during forward and backward sliding. The model parameters in each case are; **a** $\tilde{\gamma} = 4, \tilde{k} = 2, \tilde{v}_0 = 0.15$. **b** $\tilde{\gamma} = 4, \tilde{k} = 2, \tilde{v}_0 = 0.05$. **c** $\tilde{\gamma} = 2, \tilde{k} = 2, \tilde{v}_0 = 0.05$. **d** $\tilde{\gamma} = 0.5, \tilde{k} = 0.2, \tilde{v}_0 = 0.05$. **e** $\tilde{\gamma} = 0.1, \tilde{k} = 0.2, \tilde{v}_0 = 0.05$

minimum. In this case, for small velocities the tip gradually follows this minimum without making any sudden jumps. However when $\tilde{k} < 1$ the system possess multiple local minima and the tip can jump from one to another during sliding. This issue is explored further in forthcoming sections. For this simple system transition from stick-slip to continuous sliding regime occurs around $\tilde{k} = 1$. Here another important parameter is $\tilde{\gamma}$. The system shows overdamped and underdamped behavior when $\tilde{\gamma} \ll 1$ and $\tilde{\gamma} \gg 1$, respectively.

One can trace the force needed to slide the tip by calculating $\tilde{k}(\tilde{x_0} - \tilde{x})$ where $\tilde{x_0} = \tilde{v_0}\tilde{t}$ is position of the other end of the tip. The result of such calculation is presented in Fig. 21.2. Here the tip is slid forward and backward to complete a friction loop. The area covered by this loop correspond to the dissipated energy. One can see in Fig. 21.2a–c that when $\tilde{k} > 1$ the force loop is smooth which corresponds to continuous sliding. Comparing the area covered by loops presented here one can see that the friction force in continuous sliding regime is proportional to $\tilde{\gamma}\tilde{v_0}$.

Conversely, force loops having sudden changes can be seen in Fig. 21.2d, e which corresponds to stick-slip regime with $\tilde{k} < 1$. Comparing Fig. 21.2c, d one can see that

the area covered by the friction loop is much larger in (d), despite the decrease in $\tilde{\gamma}$. This shows that in stick-slip regime the friction force has much larger contribution from sudden processes compared to $\tilde{\gamma}\tilde{v_0}$ term that appear in continuous sliding regime. Another interesting phenomena is observed when Fig. 21.2d, e are compared. One can see that when $\tilde{\gamma} = 0.1$ the system is in underdamped stick-slip regime where double slips occur.

In the light of the above model the following trends are found when one looks at the variation of the average friction force $\tilde{F}$ with sliding velocity $\tilde{v_0}$. When $\tilde{k} > 1$ the average friction force linearly varies with sliding velocity and approaches zero as the velocity goes to zero. However, when $\tilde{k} < 1$ the average friction force converges to some finite value as sliding velocity approaches zero. Interestingly, when $\tilde{k}$ and $\tilde{\gamma}$ are small while $\tilde{v_0}$ is above some critical value, the system starts to show multiple slips which in turn lowers the average friction force dramatically.

21.1.4 Motivation

Advances in atomic scale friction [3–5] have provided insight on dissipation mechanisms. The stick-slip phenomena is the major process, which contributes to the dissipation of the mechanical energy through sudden or non-adiabatic transitions between bi-stable states of the sliding surfaces [1, 2, 6, 7]. During a sudden transition from one state to another, the velocities of the surface atoms exceed the center of mass velocity sometimes by orders of magnitudes [8]. Local vibrations are created thereof evolve into the non-equilibrium system phonons via anharmonic couplings [9] within picoseconds [10, 11]. In specific cases, even a second state in stick-slip can coexist [7].

In Fig. 21.1, two regimes of sliding friction are summarized within the framework of Prandtl-Tomlinson model [1, 2, 8], where an elastic tip (+cantilever) moves over a sinusoidal surface potential. The curvature of this potential at its maximum gives the value of the critical stiffness k_c. If the intrinsic stiffness of the tip k_s is higher than this critical stiffness i.e. $k_s/k_c > 1$, the total energy of the tip-surface system always has one minimum. The sliding tip gradually follows this minimum, which results in the continuous sliding regime. Conversely, if the tip is softer than the critical value, then it is suddenly slipped from one of the bi-stable states to the other. This slip event can be activated by thermal fluctuations even before the local minimum point becomes unstable [12]. Experimentally, using friction force microscope, Socoliuc et al. [13] showed that the transition from stick-slip regime to continuous sliding attaining ultralow friction coefficient can be achieved by tuning the loading force on the contact.

Superlubricant materials composed of weakly interacting two-dimensional (2D) layers have been a central figure of intense studies in tribology. In this respect, recently synthesized, two-dimensional, single layer honeycomb structures, which have been synthesized, hold the promise of being potential lubricant material between two sliding flat surfaces.

21.2 Superlubricity Between Two Layers of Graphene Derivatives and Transition Metal Dichalcogenides

Here we investigate the sliding friction between two same pristine layers of nanostructures, such as graphane, [14, 15] fluorographene, [16, 17] molybdenum disulfide, [18] and tungsten dioxide, [19] (abbreviated according to their stoichiometry as CH, CF, MoS_2 and WO_2 respectively) using the Density Functional Theory [20, 21]. We find that these nanostructures avoid stick-slip even under high loadings and execute continuous sliding. Consequently, the sliding occurs without friction that would originate from the generation of non-equilibrium phonons. Our approach mimics the realistic situation, where the total energy and forces are calculated from first-principles as two-dimensional (2D) two layers undergo a 3D sliding motion under a constant (normal) loading force. This is the most critical and difficult aspect of our study. In this respect, our results provide a 3D rigorous *quantum mechanical* treatment for the 1D and empirical Prandtl-Tomlinson model [1, 2].

The nanostructures considered in the present study are recently discovered insulators having honeycomb structure, which can form suspended single layers as well as multilayers. The unusual electronic, magnetic and elastic properties of these layers have been the subject of recent numerous studies. In particular, they have large band gaps to hinder the dissipation of energy through electronic excitation and have high in-plane stiffness ($C = (1/A)\partial^2 E_s/\partial\epsilon^2$, i.e. the second derivative of the strain energy relative to strain per unit area, A being the area of the unit cell) [17–19, 22]. Analysis based on the optimized structure, phonon and finite temperature molecular dynamics calculations demonstrate that each suspended layer of these nanostructures are planarly stable [15, 17–19]. In graphane, positively charged three hydrogen atoms from the top side and another three from the bottom are bound to the alternating and buckled carbon atoms at the corners of hexagons in graphene to form a uniform hydrogen coverage at both sides (see Fig. 21.3a). Recently synthesized CF [16] is similar to CH, but F atoms are negatively charged. Tribological properties of carbon based fluorinated structures have been the focus of interest [23, 24]. In the layers of MoS_2 or WO_2, the plane of positively charged transition metal atoms is sandwiched between two negatively charged outer S or O atomic planes. It was shown that MoS_2 structure can have ultralow friction [25]. Theoretically, the static energy surfaces are calculated during sliding at $MoS_2(001)$ surfaces [26]. Apparently, the interaction energy between two single layers of these nanostructures is mainly repulsive due to charged outermost planes except very weak Van der Waals attractive interaction around the equilibrium distance. In Fig. 21.3, each layer being a large 2D sheet consisting of three atomic planes mimics one of two sliding surfaces. In practice, sliding surfaces can be coated by these single layer nanostructures as one achieved experimentally [27].

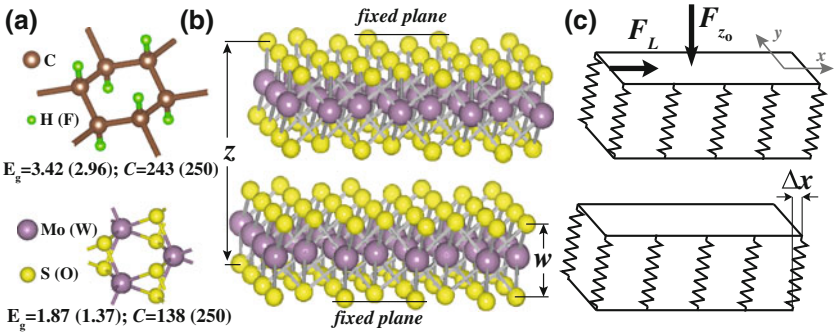

Fig. 21.3 **a** Ball and stick model showing the honeycomb structure of graphane CH (fluorographene CF) (*top*) and MoS_2 (WO_2) (*bottom*). Calculated values of energy gaps E_g and in-plane stiffness C are also given in units of eV and J/m^2 respectively. **b** Two MoS_2 layers sliding over each other have the distance z between their outermost atomic planes. **c** Each layer is treated as a separate elastic block. Lateral F_L and normal (loading) F_{z_o} forces, the shear of bottom atomic plane relative to top atomic plane in each layer $\Delta x(y)$, and the width of the layer w, are indicated

21.2.1 Methods

To investigate the sliding friction between surfaces coated with single layer nanostructures we used an approach, which is based on quantum mechanics. Our results are obtained by state-of-the-art Density Functional Theory (DFT) plane wave calculations within the Generalized Gradient Approximation (GGA) [28] including van der Waals corrections [29] and using PAW potentials [30]. All structures have been treated within supercell geometry using the periodic boundary conditions. A plane-wave basis set with kinetic energy cutoff of 400 and 500 eV is used for transition metal and carbon based structures respectively. In the self-consistent potential and total energy calculations the Brillouin zone is sampled by fine meshes. All atomic positions and lattice constants are optimized by using the conjugate gradient method where total energy and atomic forces are minimized. The convergence for energy is chosen as 10^{-5} eV between two steps, and the maximum force allowed on each atom is less than 10^{-4} eV/Å. Numerical plane wave calculations have been performed by using VASP package [31, 32]. Further details of the calculations can be obtained from the [33, 34].

21.2.2 Critical Curvature

We consider two layers of the same nanostructures in relative motion, where the spacing z between the bottom atomic plane of the bottom layer and the top atomic plane of the top layer is fixed. These layers mimics two surfaces coated by these nanostructures. These layers mimics two surfaces, which are coated by Here the

frictional behavior of the system is dictated mainly by C–H(F), Mo–S and W–O bonds and their mutual interactions. These layers are represented by periodically repeating rectangular unit cells. We calculate the value of the equilibrium lattice constants, which increase as z decreases. For each value of z the fixed atomic layer at the top is displaced by x and y on a mesh within the quarter of the rectangular unitcell. Then all possible relative positions (displacements) between fixed atomic layers are deduced using symmetry. At each mesh point all atoms of the system except those of fixed top and bottom planes are relaxed and the total energy of the system $E_T(x, y, z)$ (comprising both layers) is calculated. We have also derived $\Delta x(x, y, z)$ and $\Delta y(x, y, z)$ data which correspond to the shear (deflection) from the equilibrium position of the relaxed atomic planes relative to the fixed atomic plane of the same layer as illustrated in Fig. 21.3c. The matrices of these data are arranged for each nanostructure using the mesh spacing of ∼0.2 Å in x and y directions. The forces exerting on the displacing top layer in the course of relative motion of layers are calculated from the gradient of the total energy of the interacting system, namely $F(x, y, z) = -\nabla E_T(x, y, z)$ at each mesh point (x, y). These forces are in agreement with the resultant of the atomic forces calculated for the top layer using Hellman-Feynman theorem. Eventually, the matrices of all data, namely $E_T(x, y, z)$, $\Delta x(x, y, z)$, $\Delta y(x, y, z)$ and $\mathbf{F}(x, y, z)$ are made finer down to mesh spacing of ∼0.05 Å using spline interpolation.

The properties affecting the friction between layers should be derived under a given constant loading force. First of all we preset the value of applied loading, F_{z_o}, which corresponds to the operation pressure when divided by the cell area A, namely $\sigma_N = F_{z_o}/A$. We obtain the normal force from $F_z(x, y, z) = -\partial E_T(x, y, z)/\partial z$ and for each x and y we calculate the value of z where $F_z(x, y, z) = F_{z_o}$ and abbreviate it as $z_o(x, y)$. Then by using spline interpolation in z direction we calculate the x and y dependence of $F_{x_o}[x, y, z_o(x, y)]$ and $F_{y_o}[x, y, z_o(x, y)]$, as well as $\Delta x_o[x, y, z_o(x, y)]$ and $\Delta y_o[x, y, z_o(x, y)]$ for a given F_{z_o}. The lateral force is then $\mathbf{F}_L[x, y, z_o(x, y)] = F_{x_o}\hat{i} + F_{y_o}\hat{j}$. Integrating the lateral force over the rectangular unitcell we obtain,

$$E_I[x, y, z_o(x, y)] = \int_0^x \int_0^y \mathbf{F}_L(x, y, z_o(x, y)) \cdot \mathbf{dr} \tag{21.3}$$

where $E_I[x, y, z_o(x, y)]$ is the interaction energy for displacement (x, y) in the cell under applied constant loading force F_{z_o}. It should be noted that E_I is different from $E_T(x, y, z)$ (but $E_I \to E_T$ for $z \gg 1$) and is essential to reveal the friction coefficient. Contour plots of E_I of two sliding MoS_2 layers calculated for $\sigma_N = 15$ GPa are shown in Fig. 21.4a and those of CH, CF, WO_2 in Fig. 21.5a. The profile of E_I is composed of hills arranged in a triangular lattice. These hills correspond to the relative positions when the charged atoms of adjacent layers have the minimum distance. The hills are surrounded by two kind of wells. The difference between these two wells is enhanced with increasing pressure. The wells form a honeycomb

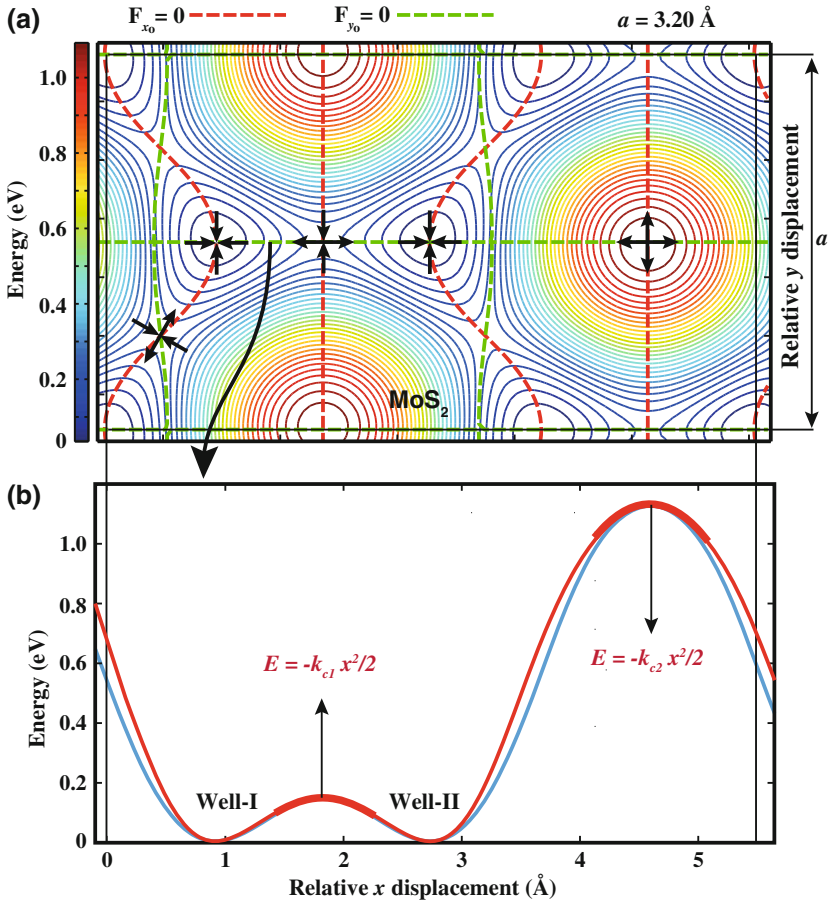

Fig. 21.4 **a** The contour plot of interaction energy E_I of two sliding layers of MoS_2. The zero of energy is set to $E_I[0, 0, z_o(0, 0)]$. The energy profile is periodic and here we present the rectangular unitcell of it. The width of this unitcell in y-direction is equal to the lattice constant a of the hexagonal lattice. Forces in x- (y-) direction is zero along the *red* (*green*) dashed lines, respectively. There are several points at which the lateral force $\mathbf{F_L}$, is zero. The arrows at these critical points indicate the directions where the energy decreases. **b** The energy profiles of E_I (*blue line*) and E_I^o (*red line*) along the *horizontal line* with $F_y = 0$ for MoS_2. Loading pressure in all cases is $\sigma_N = 15$ GPa

structure and are connected to each other through the saddle points (SP). When the layers are moved over each other they will avoid the relative positions corresponding to the hills. For example, if the layers are pulled in the y-direction they will follow the curved $F_x = 0$ path passing through the wells and SP but not the straight one passing through the hills as shown in the Fig. 21.4b. This makes SP very important because moving from one well to the adjacent one requires to overcome the barriers at these points. We note that the critical stiffness can be calculated from the curvature of E_I^o, which is obtained by subtracting the strain energies of two sliding MoS_2 layers,

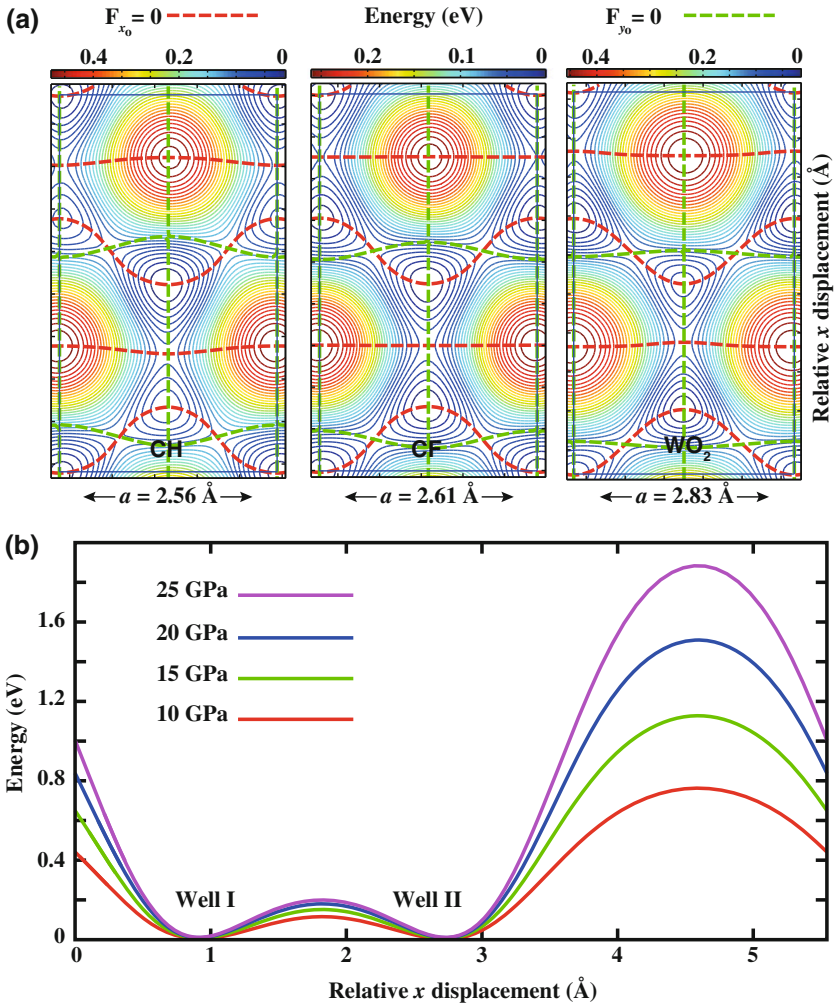

Fig. 21.5 **a** Contour plots of interaction energy E_I of two layers of CH, CF, and WO_2 executing sliding motion under constant loading pressure are presented in their rectangular unit cells. The zero of energy is set to $E_I[0, 0, z_o(0, 0)]$. Loading pressure in all cases is $\sigma_N = 15$ GPa. **b** Variation of interaction energy E_I^0 with applied loading for MoS_2 structure along the straight $F_y = 0$ line passing through two wells, saddle point and one hill

namely $E_I^o = E_I - k_s(\Delta x_o^2 + \Delta y_o^2)$ and by replacing x by $x - 2\Delta x_o$. While the SP serves as a barrier in the direction joining the nearby wells it acts as a well in the perpendicular direction joining the hills. Since we are interested in the curvature of the SP in the former direction we have made a plot along the $F_y = 0$ line which passes through the hill, the wells and the SP in between as shown in the Fig. 21.4b. We derive two critical stiffness values from E_I^o curve for a given normal loading

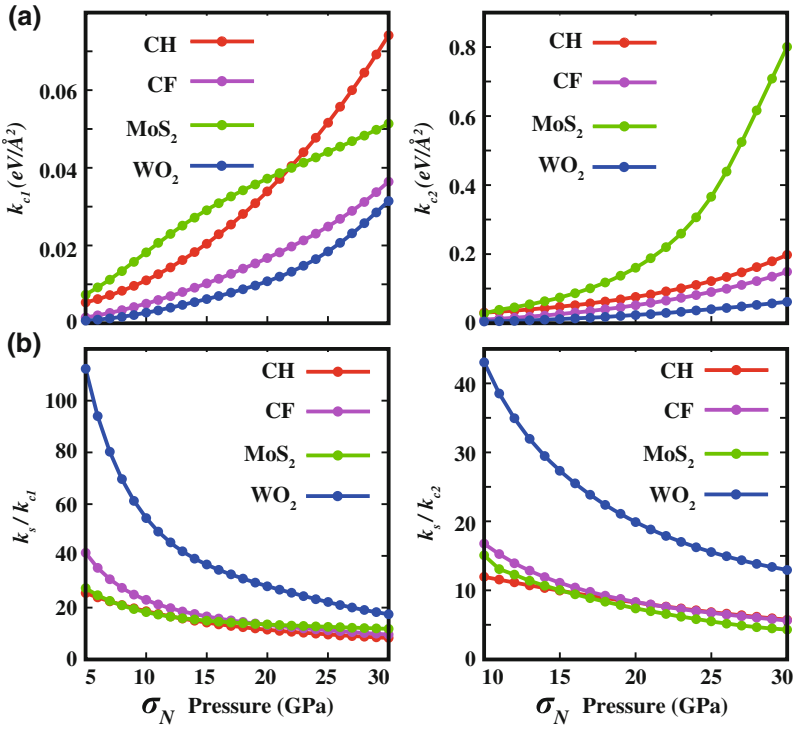

Fig. 21.6 **a** The variation of k_{c1} and k_{c2} with loading pressure. **b** The variation of the frictional figures of merits k_s/k_{c1} and k_s/k_{c2}, with loading pressure calculated for CH, CF, MoS_2 and WO_2

force; namely k_{c1} at the SP and k_{c2} at the hill by fitting the curve at the maxima of the barriers to a parabola. Although the hills will be avoided during sliding motion the curvature at these points are calculated for completeness. We also present the variation of E_I^0 with applied loading for MoS_2 structure in Fig. 21.5b. Note that, the variation of the amplitude at the saddle point is minute. In Fig. 21.6a the variation of k_{c1} and k_{c2} of CH, CF, MoS_2 and WO_2 with loading pressure σ_N is presented. Generally, the critical stiffness, in particular k_{c1} is low due to repulsive interaction between sliding layers. This facilitates the transition to continuous sliding.

21.2.3 Intrinsic Stiffness

Next we calculate the intrinsic stiffness k_s of individual MoS_2 layers using the force and the displacement data. For each x and y the lateral forces $F_{x_o}[x, y, z_o(x, y)]$ and $F_{y_o}[x, y, z_o(x, y)]$ versus the displacements $\Delta x_o[x, y, z_o(x, y)]$ and $\Delta y_o[x, y, z_o(x, y)]$, respectively are plotted. As shown in Fig. 21.7, this data falls on a straight

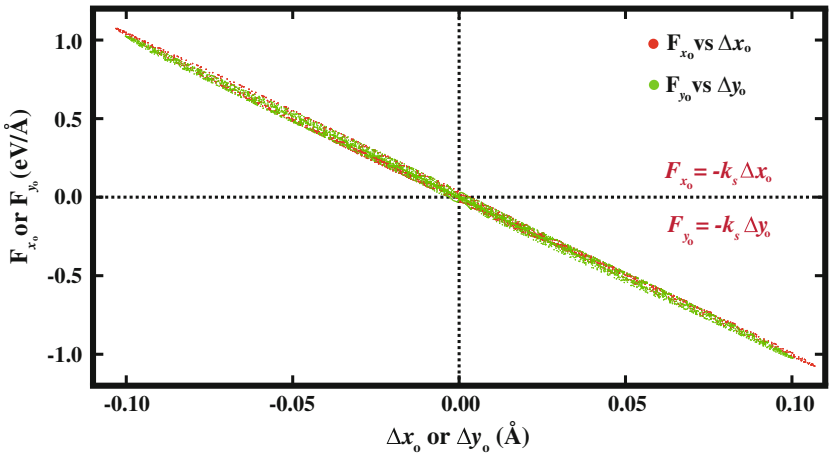

Fig. 21.7 The force versus shear values along x- and y-directions for each mesh point by *red* and *green dots*, respectively

line having a negative slope as expected from Hook's law of elasticity. We note that the elastic properties of layers having honeycomb structure is uniform and is independent of the direction of displacement and force [22]. The magnitude of the slope, $k_s = -F_{x(y)_o}/\Delta x(y)_o$ gives us the stiffness of the layers. Note that, normally the stiffness is defined as stress over strain and has units of energy per volume. Here we only need the ratio of material stiffness to the critical stiffness and should have the same units. The critical stiffness was calculated as second order spatial derivative of energy in the unitcell and it has units of energy per unitcell per unit area. As defined above, the stiffness of layers, k_s, also has units of energy per unitcell per unit area. Calculated intrinsic stiffness values of CH, CF, MoS_2 and WO_2 in the range of σ_N from 5 to 30 GPa are found to be 6.15 ± 0.15, 4.5, 10.0 ± 0.3 and 15.2 ± 0.3 eV/Å^2, respectively. Clearly, these values of k_s, in particular those of MoS_2 and WO_2 are rather high.

21.2.4 Frictional Figure of Merit

Based on the discussion at the beginning, the ratios k_s/k_{c1} and k_s/k_{c2} give us a dimensionless measure of performance of our layered structures in sliding friction. When these ratios are above two (since both layers in relative motion contribute), the stick-slip process is replaced by continuous sliding, whereby the dissipation of mechanical energy through phonons is ended. Under these circumstances the friction coefficient diminish, if other mechanisms of energy dissipation were neglected. For this reason one may call these ratios as a frictional figures of merit of the layered materials. In Fig. 21.6b we present the variations of the ratios k_s/k_{c1} and k_s/k_{c2} with

normal loading forces. Even for very large σ_N, $k_s/k_{c1} > 2$ and $k_s/k_{c2} > 2$. For usual loading pressures, the stiffness of MoS_2, CF and CH is an order of magnitude higher than corresponding critical values. Interestingly, for WO_2 this ratio can reach to two orders of magnitudes at low pressures. The absence of mechanical instabilities has been also tested by performing extensive simulations of the sliding motion of layers in very small displacements. C–H, C–F, Mo–S and W–O bonds in each case of two layers in relative motion under significant loading force did not display the stick-slip motion.

21.2.5 Stick-slip in Silicane: A Counter Example

Conversely, we now examine the sliding of two silicane [35, 36] layers (abbreviated as SiH and composed of silicene [37] saturated by hydrogen atoms from both sides, like graphane) with $k_s = 2.1 \pm 0.1$ eV/Å^2 for 2 GPa $\leq \sigma_N \leq$ 8 GPa. This is an interesting material because the onset of stick-slip occurs already at low loading pressures and exhibits a pronounced asymmetry in the direction of sliding between two wells. In Fig. 21.8 we present the lateral force variation calculated for two different loading pressures. For small loading pressure, σ_N=2 GPa the stick-slip is absent since approaching the SP from Well-I, the curvature is $k_{c,I} = 0.28$ eV/Å^2 and from Well-II it is $k_{c,II} = 0.16$ eV/Å^2, thus $k_s/k_{c,I or II} > 2$ for both directions. Whereas, once the pressure is raised to $\sigma_N = 8$ GPa stick-slip already governs the sliding friction, since $k_{c,I}$ reaches 1.38 eV/Å^2. Interestingly, since $k_{c,II}$ is only 0.28 eV/Å^2 for $\sigma_N = 8$ GPa, going from Well-II to Well-I a slip event occurs at SP. Eventually, one sees in Fig. 21.8 a hysteresis in the variation of F_L leading to energy dissipation.

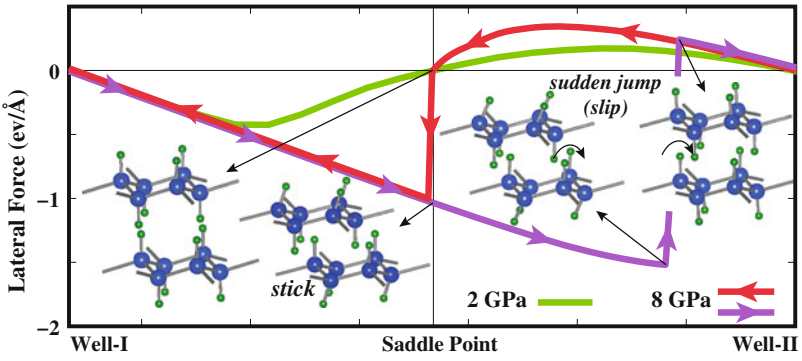

Fig. 21.8 Calculated lateral force variation of two single layer SiH under two different σ_N. The *top layer* is moving to the *right* or to the *left* between two wells. Atomic positions of two SiH layers in stick and slip stages are shown by inset. The movement of SiH layers under loading pressure of $\sigma_N = 8$ GPa is presented as a supplemental material of our work [33]

21.3 Superlubricity Between Graphene Coated Metal Substrates

Bulk counterparts of molybdenum disulfide and graphite flakes were used as a solid lubricant in industrial applications long before the 2D layers constituting them were isolated. The key features which make these materials so important in friction science are strong covalent intralayer bonds in contrast to weak van der Walls interlayer interactions. As discussed in the previous sections, the contrast between these intralayer and interlayer interactions can be quantified in terms of frictional figure of merit [33].

Experimental and theoretical studies have shown that friction force between graphite layers can be very small when the layers are slid with a certain angle to each other [38, 39]. In this case the rotated layers are incommensurate with respect to each other and the corrugation potential between such layers is flat. It was shown that, the torque felt by rotated layers can twists them until the layers become commensurate which increases the friction force [40]. Transition between commensurate and incommensurate states of graphene flakes on graphite was investigated in detail by several theoretical studies [41–43].

Recently, several experimental works investigated the variation in friction force when the number of 2D layers are varied from single layer to many layers representing the bulk structure [44–46]. Lee et al. used friction force microscope with a SiN tip to investigate atomic friction on graphite and graphene flake prepared on silicon oxide layer [44]. They have found that friction on graphene was lower than on silicon oxide but higher than that on graphite. Their results show that friction force monotonically decreases as the number of graphene layers are increased and approaches the bulk value found for graphite. They have attributed this trend to long ranged van der Walls interactions between layers.

Filleter et al. used atomic force microscope with cantilevers coated in a polycrystalline diamond film and found that friction force on single layer graphene epitaxially grown on SiC is lower than that on SiC surface but higher than bilayer graphene on SiC [45]. In contrast to other works, they have found the friction force to be higher on graphite compared to bilayer graphene. They have found the similar trends when oxidized single crystal silicon cantilevers with sharper tips were used. They assert that, the lower friction measured in bilayer graphene is related to suppressed electron-phonon coupling which plays important role in dissipation.

Much recently, the variation of friction force with number of layers was investigated for structures composed of graphene, molybdenum disulfide, niobium diselenide and hexagonal boron nitride layers [46]. Similar to results of Lee et al., it was found that the friction force decreases as the number of layers increase. It was also found that, this trend continues to be observed in suspended layers while it is suppressed when graphene layers are deposited on highly adherent mica surface. Here the observed trend was attributed to higher compliance of thin layers to perpendicular stress. Together with finite element simulations they show that as the tip is slid over, the layers are puckered and piled up in direction of sliding, which increases the contact area and resistance to sliding. The puckering is more pronounced when

the number of layers are decreased. Due to similar reasons, the trend is suppressed in mica because it prevents graphene layers from puckering.

The potential of graphene as a lubricant material can be revealed realistically, when it is placed between two flat sliding surfaces. Here we investigate the energy dissipation and the strength of the potential corrugation between two Ni(111) surfaces having $n = 0 - 5$ layers of graphene in between. We treat infinite surfaces using periodic boundary conditions, which also minimizes effects such as puckering or rippling [46]. Our approach mimics a realistic situation where the metallic surfaces are coated by graphene layers and the radii of asperities are much larger compared with atomic scales. Similar to what detailed in the previous section, the interaction energy, as well as lateral forces are calculated using quantum mechanical treatments as 2D layers execute a 3D sliding motion under a given constant normal force. We found that strong adhesive forces between Ni(111) surfaces, which lead to strong energy dissipation and wear are substantially suppressed when a single layer of graphene is inserted between the surfaces. However, the system enters into the continuous sliding regime only after the second layer of graphene is inserted, whereby each graphene layer becomes attached to one Ni(111) surface. Even more interesting is that inserting more graphene layers between Ni(111) surfaces decreases the friction gradually. On the other hand, the friction between graphene layers sliding over each other are larger and practically independent of the number of layers n in between, when the supporting Ni surfaces are not present. These results reveal the capacity of graphene as a superlubricant leading to nearly frictionless sliding and are explained by a charge exchange mechanism between graphene and Ni slabs.

21.3.1 Model and the Atomic Structure

The frictional properties of graphene layers sandwiched between Ni(111) surfaces and those of bare graphenes are treated using the models described in Fig. 21.9. In all calculations sliding nickel surfaces are represented by slabs consisting of three atomic layers of bulk Ni. We apply periodic boundary conditions along the plane parallel to the surfaces with a primitive unitcell comprising one Ni and two C atoms in each layer. The interaction between periodic images of Ni slabs is hindered by introducing a vacuum spacing of 15 Å. The structure presented in Fig. 21.9a is named as Ni-ABCBA-Ni structure, where A, B, and C correspond to certain in-plane configuration of carbon atoms. To avoid any confusion the atomic layers comprising the Ni slabs are arranged in a mirror symmetry. This arrangement is presented in Fig. 21.9a, while the in-plane configuration of Ni and C atoms in each plane is shown in Fig. 21.9b. Nickel atoms positioned at the bridge sites of graphene structure attracts C atoms and slightly breaks the honeycomb symmetry, as shown in Fig. 21.9b. The nature of this interaction is discussed in forthcoming parts in detail. The equilibrium positions of Ni and C atoms are attained by structure optimization at a given constraint. Details of calculations are given in Sect. 21.2 and in [34].

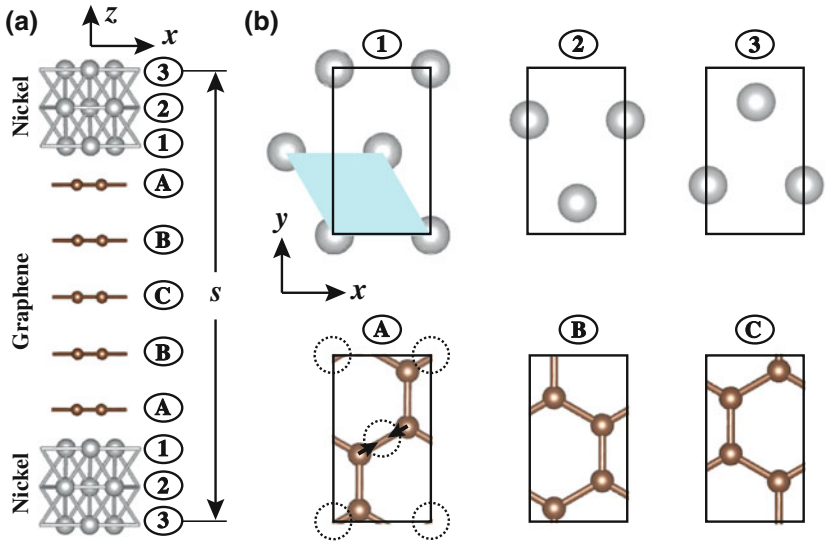

Fig. 21.9 **a** *Side view* of the arrangement of the Ni-ABCBA-Ni structure. The outermost Ni(111) atomic planes are fixed at the separation s. **b** *Top view* of individual layers constructing the Ni-ABCBA-Ni structure. The primitive unitcell is shown by *blue shaded area*. *Dotted circles* represent optimized positions of Ni atoms below the graphene layers in configuration A

21.3.2 Adhesion Hysteresis

We start our analyses by calculation of forces on outermost atoms of Ni slabs when they are kept fixed during the relaxation while the separation, s, between them (see Fig. 21.9a) is gradually varied. We start by two Ni slabs each composed of three atomic layers with no graphene in between. The dashed green curve shown in Fig. 21.10a is obtained when s is gradually decreased. One can observe a slightly attractive region followed by a sudden increase in the attractive force after which the force starts to decrease until the equilibrium distance is reached and the force becomes repulsive. During the sudden increase in attractive force both layers are elongated towards each other and after this stage the distance between the facing atomic layers remain nearly constant until the equilibrium is reached. The red solid line in Fig. 21.10a shows the variation of forces when s is gradually increased. This time, the curve takes a different route right at the point where the sudden increase of the attractive force was observed. When s is increased further the facing two layers detach from the slabs and attach to each other. The observed hysteresis manifests the adhesion and wear phenomena frequently observed between metallic contacts.

Next we insert one graphene layer in the minimum energy configuration A described in Fig. 21.10b between two Ni slabs. This graphene layer screens the interaction between Ni surfaces and significantly decreases the attractive potential between them, however the hysteresis is still present, as seen in Fig. 21.10b. We also

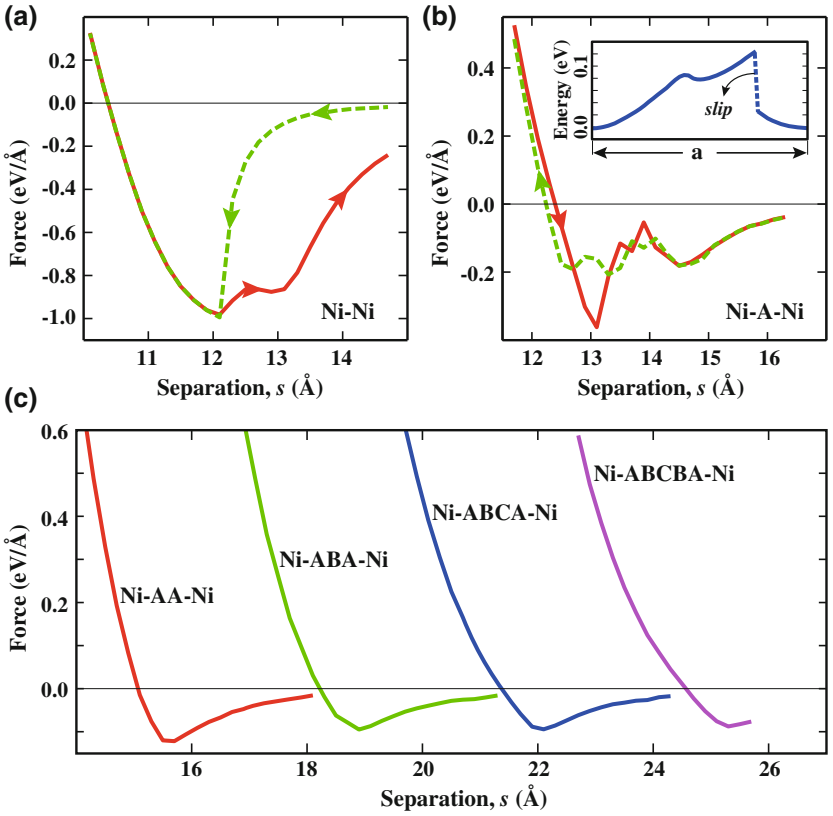

Fig. 21.10 Adhesion hysteresis curves for **a** Ni–Ni and **b** Ni-A-Ni structures and its stick-slip behavior shown by inset. **c** Normal force along z axis as a function of separation s for Ni-graphene-Ni structures with 2–5 graphene layers

observe stick-slip behavior when the Ni slabs are laterally moved relative to each other with one layer graphene in between making sudden jumps. As illustrated by inset in Fig. 21.10b, the sudden variation of energy in constant height mode demonstrates the presence of stick-slip motion causing the dissipation of mechanical energy.

When the second graphene layer is inserted, each layer becomes attached to Ni(111) surface. Under these circumstances the hysteresis is completely removed and the attractive forces are weakened. Further increasing the number of layers shows minor changes as seen in Fig. 21.10c. From these observations we deduce that, inserting single layer graphene can protect the Ni layer from wear during sliding, however one layer is not enough for the onset of the continuous sliding regime. It becomes possible only by including a second layer of graphene whereby each Ni slab is coated by graphene.

21.3.3 Trends in Multilayers

To investigate the effect of including more layers on the potential corrugation during the sliding of the layers under constant pressure, we first calculate the total energies E_T when outermost Ni layers are kept fixed at various relative lateral (x, y) positions and at fixed separation s [33]. These calculations are performed in a 3D grid of x, y, s. The distances between the data points were taken to be $\sim$0.2 Å in the lateral plane and 0.2 Å in perpendicular axis i.e s, which is then made finer down to $\sim$0.05 Å by spline interpolation. We also generate F_x, F_y and F_z matrices from the gradient of the total energy $F_{x,y,z} = -\partial E_T(x, y, z)/\partial x, y, z$, which is consistent with Hellmann-Feynman forces calculated on fixed atoms of outermost planes. We then retrieve F_x and F_y corresponding to a given F_z (normal pressure) at each (x, y) in the unit cell and generate the profiles of potential corrugation from $\int F_x dx + F_y dy$, where the minimum of total energy is set to zero. The profiles (contour plots) of potential corrugation calculated for Ni-AA-Ni and AA i.e. two flat graphene layers without Ni(111) are shown in the top and bottom panels of Fig. 21.11a, respectively. We note that the amplitude of the potential corrugation (i.e. the difference between the

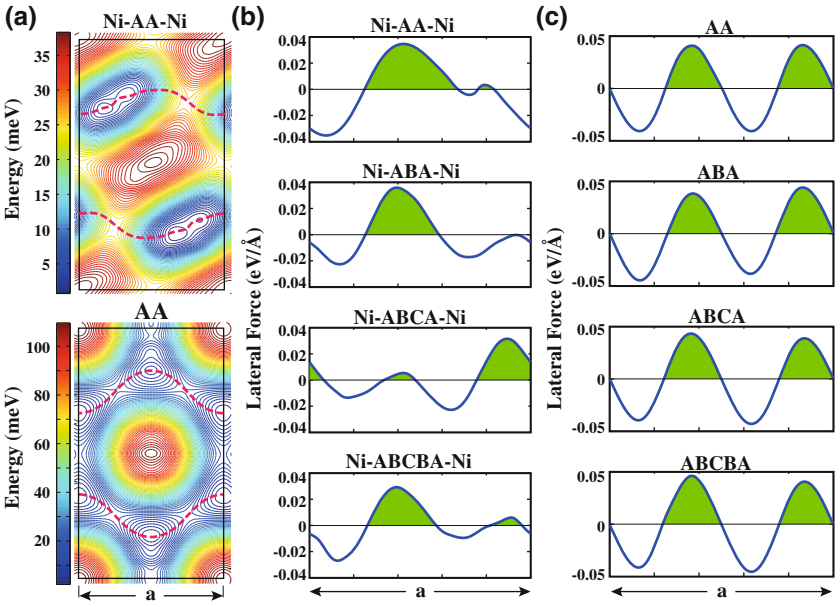

Fig. 21.11 **a** Profiles (contour plots) of potential corrugation for Ni-AA-Ni and AA [without Ni(111) slabs] structures calculated for constant pressure of 7 GPa. The paths along which one slab moves in the course of sliding when pulled along x axis are shown by *red dashed lines*. The lattice constant of the unit cell is indicated by a. **b** Variation of lateral force F_x along x-axis during sliding of Ni-AA-Ni structures over the path shown in (**a**). The sum of areas shaded in green is defined as the corrugation strength W_D (see text). **c** Same as (**b**) for sliding AA structures without Ni(111) slabs

minimum and maximum of energy) is an order of magnitude smaller compared to single-layer honeycomb structures of graphane CH, fluorographene CF, MoS_2 and WO_2 discussed in precious section. On the other hand, the intrinsic stiffness of the present case, which is related to the interaction between Ni and graphene layers is also substantially lower ($k_s = 0.8$ eV/A^2) compared to the intrinsic stiffness of those honeycomb structures [33]. The lower intrinsic stiffness accompanied by low potential corrugation curvature results in a frictional figure of merit of $\sim$10, at constant pressure of 7 GPa, which is enough to keep the system in continuous sliding regime. Comparing the profiles of the potential corrugation of Ni-AA-Ni and AA structures, one can see how the interaction between graphene layers is affected by their interaction with Ni surfaces. The effect of distortion presented in Fig. 21.9b is reflected to the potential corrugation of Ni-AA-Ni, since its symmetry is changed from hexagonal to rectangular. Also note that, the amplitude of the potential corrugation is substantially lowered when Ni slabs are present, which reveals an important effect of substrate (i.e. Ni(111) surface).

To set a measure for the corrugation strength we first derive the path at which the upper slab would slide if it was pulled along x-axis. This path is shown by dashed lines in Fig. 21.11a for the case of Ni-AA-Ni. In the case of structures having more than two graphene layers the path is found directly by starting from the Ni slab positions presented in Fig. 21.9 and moving along the x-axis while minimizing the total energy along y axis. Then we calculate the lateral force F_x along x-axis felt by the slab, as shown in Fig. 21.11b. Here we note that in the sliding of Ni(111) slabs having n graphene layers the dissipation of energy through non-equilibrium phonons generated by sudden processes is hindered for $n \geq 2$ and hence $W = \int_0^a F_x dx$ vanishes. This, however, does not precludes energy dissipation through other mechanisms. With a premise that the maximum of the energy to be dissipated by any mechanism should be smaller than $W_D = \int_0^a F_x^> dx$ i.e. the integral of all positive work done during sliding of one slab over one unitcell shown by the green shaded region in Fig. 21.11b, we took W_D as a measure for the corrugation strength. The result of these calculations are presented in Fig. 21.11b. Note that W_D (is also related to kinetic friction coefficient $\mu_k = (W_D/a)/F_z$) is already very small. To check the effect of the type of stacking we have also calculated the force variation for Ni-ABABA-Ni structure and the result was very close to that of Ni-ABCBA-Ni structure. For comparison, we have performed the same calculations for graphene layers in the same stacking but without Ni slabs above. The results of these calculations are presented in Fig. 21.11c.

Various important trends in the corrugation strength W_D, obtained from above calculations are presented in Fig. 21.12a. As expexted the corrugation strength increases with increasing normal force. Also the corrugation strength is higher in structures composed of only graphene layers (like ABA) compared to the ones having Ni slabs (like Ni-ABA-Ni). This effect is mirrored in the repulsive interaction of graphene layers in the presence and absence of Ni slabs, as shown in Fig. 21.12b. Here one can see that introducing Ni slabs decreases the repulsive interaction between graphene layers, which is consistent with decrease in the corrugation strength discussed above. Another important finding is that corrugation strength of the structures solely

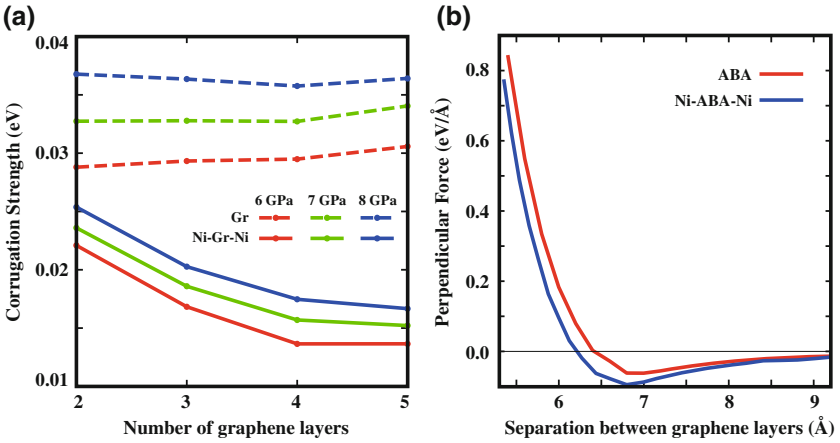

Fig. 21.12 **a** Variation of the corrugation strength with number of layers as a function of applied loading pressure for n number of graphene layers (with and without Ni(111) substrates). **b** Perpendicular force F_z versus the separation distance between outermost graphene layers for Ni-ABA-Ni and ABA structures ($n = 3$). In the repulsive range, the perpendicular force and hence the potential corrugation is larger in the absence of Ni(111) slabs

composed of graphene layers has minor variation with the number of layers. On the other hand, the corrugation strength is significantly decreased when the number of graphene layers in Ni-graphene-Ni structures are increased. This trend is seemingly in accordance with experimental observations [44, 46]. However, as mentioned above, the system at hand is very different from those considered in the experiments and the trends revealed by Fig. 21.12a heralds another important effect.

21.3.4 Analysis of Charge Density

To explain these trends we first examine the effect of Ni slabs on the electronic structure of graphene layers. The self-consistent difference charge density $\Delta\rho$, is obtained by subtracting the charge density of ABA structure and two Ni(111) slabs from that of Ni-ABC-Ni structure. The isosurfaces of $\Delta\rho$ and the variation of its value averaged over (x, y)-planes parallel to graphene layers (called linear density) are presented in Fig. 21.13. The major charge transfer is between Ni and graphene layers attached to each other as seen in top and middle panels of Fig. 21.13. The dangling Ni-d_{z^2} orbitals at the surface of the slab change their character upon coating of graphene layers. This is resulted in the charge depletion denoted by the numerals 1 and 3 in the linear charge density plot. Analysis of the band structure show significant contribution to C-p_z states from s, d_{xz} and d_{yz} orbitals of Ni atoms, while C-p_z orbitals by themselves contribute to d_{xy} and d_{x^2} states of Ni atoms. As a result of these complex mechanism of charge transfer the charge density around the graphene

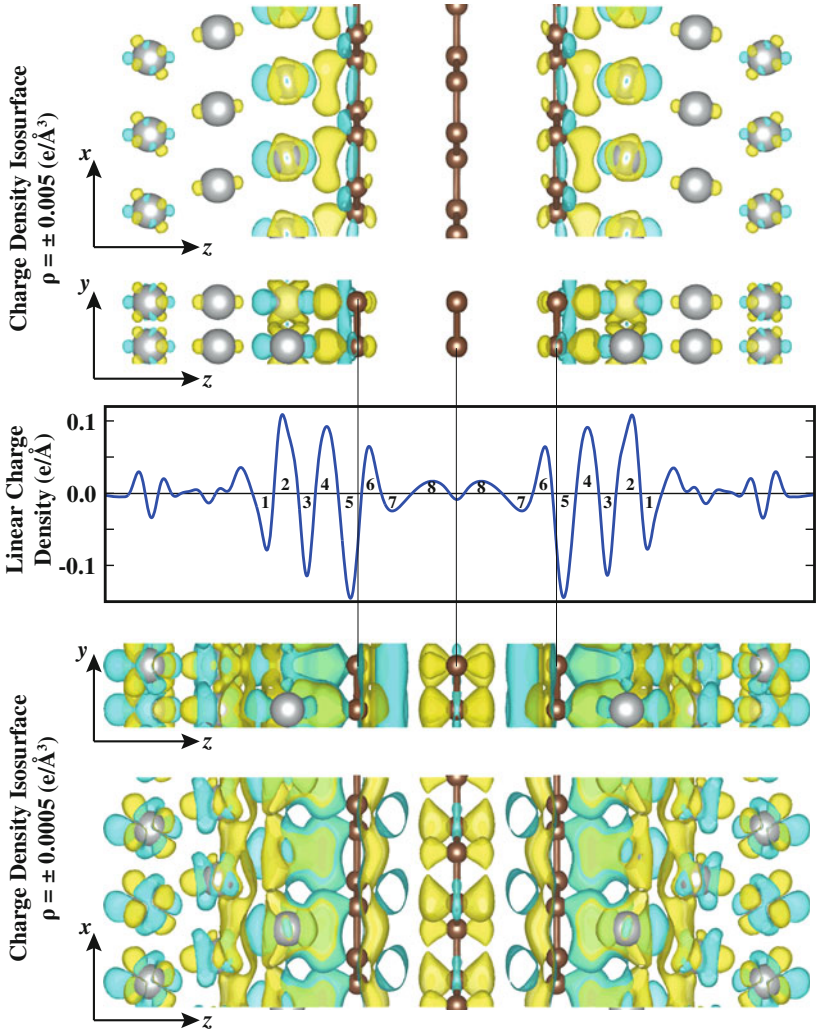

Fig. 21.13 Isosurfaces and variation of linear density of charge density difference along z-axis. The difference charge density is obtained by subtracting the charge densities of Ni slabs and ABA structures from the charge density of Ni-ABA-Ni structure at ∼6 GPa. *Yellow* (*blue*) isosurface plots correspond to the charge density accumulation (depletion). Specific regions of depletion and accumulation is denoted by numerals on the linear density of charge density difference plot

layer is shifted towards Ni slab resulting in charge density accumulations (depletions) denoted by numerals 4 and 6 (5 and 7).

The charge density depletion denoted by numeral 7 in the linear density of charge difference may be the key feature to explain the decrease in the corrugation strength between graphene layers due to Ni slabs. The isosurface of charge depletion

corresponding to this region can be seen in the bottom panel of Fig. 21.13. This charge depletion lowers the chemical interaction between graphene layers and results in lowering of corrugation strength as seen in Figs. 21.11 and 21.12. Moreover, similar charge depletions are also observed in Ni-AB-Ni, Ni-ABCA-Ni and Ni-ABCBA-Ni structures and their amplitude asymptotically increases by going from two to five layers. This is in accordance with the decrease in the corrugation strength with increasing number of layers, shown in Fig. 21.12b.

In summary, we find that even in the present model, where graphene layers have negligible puckering, the corrugation strength is decreased upon coating of the sliding Ni surfaces and increasing the number of layers. This is attributed to a complex charge transfer between graphene layers and Ni(111) surfaces, each coated by these graphenes. This transfer results in charge depletion between graphene layers thereby decreasing the corrugation strength. In the absence of Ni slabs each coated by a graphene layer, the corrugation strength is relatively higher and practically independent of the number of graphene layers. Our results demonstrate that graphene attached to sliding surfaces operate as superlubricant by suppressing energy dissipation dramatically.

21.4 Discussions and Conclusions

In conclusion, using a criterion for the transition from stick-slip to dissipationless continuous sliding regime, which is calculated from the first-principles, we showed that a pair of sliding layer of the same nanostructures, such as pairs of CH, CF, MoS_2 and WO_2, execute continuous sliding with ultralow friction. The minute variation of the amplitude of the interaction potential due to the repulsive interaction, as well as stiff C–H(F), Mo–S and W–O bonds underlie the frictionless sliding predicted in the present study. Our predictions put forward an important field of application as ultralow friction coating for the layered honeycomb structures, which can be achieved easily to hinder energy dissipation and wear in sliding friction. Earlier, the sliding motion of the diamond like carbon coatings exposed to hydrogen plasma resulted in a very low friction coefficient [47]. Ultralow friction was attributed to repulsive Coulomb forces between DLC films facing each other in sliding. However, when exposed to open air in ambient conditions, positively charged H atoms was replaced by negatively charged O and hence the uniformity in the charging was destroyed. In the present study, graphane coating is reminiscent of the hydrogenated DLC and accordingly is found to have ultralow friction, but vulnerable to degradation by oxygen atoms. Unlike graphane and DLC coating, WO_2 coating consists of negatively charged oxygens and hence immune to oxidation.

We showed that even if the strong interaction between the sliding surfaces of Ni(111) is dramatically reduced by a single layer graphene placed in between, the bistability between approach and pull-off remains. Also the stick-slip motion still exists and continues to dissipate significant amount of mechanical energy. The stick-slip motion and hence the generation non-equilibrium phonons are eliminated with

the onset of continuous sliding, once each of metal surfaces in relative motion is coated by a single graphene layer. This is attributed to substantial interaction between Ni surface and graphene through complex charge exchange causing to the reduction of the chemical interaction between graphene layers and hence to the decrease of the corrugation strength. The corrugation strength continues to decrease gradually with increasing graphene layer and eventually saturates at a small value. In the absence of metal slabs each coated by a graphene layer, the corrugation strength is relatively higher and practically independent of the number of graphene layers. Our results demonstrate that graphene attached to sliding surfaces operate as superlubricant. One expects to achieve similar lubrication effect but in lesser degree by placing graphene flakes between sliding or rolling Ni(111) surfaces. The interaction between Ni(111) and graphene investigated in this study appears to be important not only for the growth of pristine graphene or for the protection from oxidation, but also for achieving the nearly frictionless friction. Easy growth of graphene on Ni(111) surfaces makes Ni also an attractive substrate for nanotribology applications. Our calculations showed that graphene layers placed between pairs of Al(111) and Cu(111) have the capacity of reducing adhesion and sliding friction. Recent tribological test results for a few layer graphene placed between sliding 440C steel surfaces revealed that wear is decreased by almost 4 orders of magnitude and friction coefficient is decreased by 5 orders of magnitude [48, 49]. These experimental results corroborate the conclusions of our present theoretical work.

Finally, we note that the first-principles calculations of potential corrugations calculated in the constant force mode are achieved by optimizing atomic structure. This way, the elastic deformations of sliding surfaces under perpendicular loading force are taken into account. We believe that this important feature of the present method will be used in future studies dealing with the development of lubricant single layer materials.

Acknowledgments This Chapter is partially based on the doctoral thesis work of S. Cahangirov at Bilkent University and the related research results were initially reported in Phys. Rev. Lett. **108**, 126103 (2012) and Phys. Rev. B. **87**, 205428 (2013). The authors thank C. Ataca, M. Topsakal, H. Şahin and Ongun Özçelik for their contributions to the theoretical research on sliding friction in our group at UNAM, National Nanotechnolgy Research Center at Bilkent University.

References

1. L. Prandtl, Z. Angew, Math. Mech. **8**, 85 (1928)
2. G.A. Tomlinson, Philos. Mag. **7**, 905 (1929)
3. B.N.J. Persson, *Sliding Friction: Physical Principles and Applications* (Springer, Berlin, 1998)
4. M. Urbakh, E. Meyer, Nature Mat. **9**, 8 (2010)
5. C.M. Mate, G.M. McClelland, R. Erlandsson, S. Chiang, Phys. Rev. Lett. **59**, 1942 (1987)
6. D. Tomanék, W. Zhong, H. Thomas, Europhys. Lett. **15**, 887 (1991)
7. A. Buldum, S. Ciraci, Phys. Rev. B **55**, 2606 (1997)
8. M.H. Mueser, M. Urbakh, M.O. Robbins, Advances. Chem. Phys. **126**, 187 (2003)
9. V.L. Gurevich, *Transport in Phonon Systems* (North-Holland, Amsterdam, 1986)

10. A. Buldum, D.M. Leitner, S. Ciraci, Phys. Rev. B **59**, 16042 (1999)
11. H. Sevincli, S. Mukhopadhyay, R.T. Senger, S. Ciraci, Phys. Rev. B **76**, 205430 (2007)
12. E. Gnecco, R. Bennewitz, T. Gyalog, Ch. Loppacher, M. Bammerlin, E. Meyer, H.-J. Gntherodt, Phys. Rev. Lett. **84**, 1172 (2000)
13. A. Socoliuc, R. Bennewitz, E. Gnecco, E. Meyer, Phys. Rev. Lett. **92**, 134301 (2004)
14. D.C. Elias, R.R. Nair, T.M.G. Mohiuddin, S.V. Morozov, P. Blake, M.P. Halsall, A.C. Ferrari, D.W. Boukhvalov, M.I. Katsnelson, A.K. Geim, K.S. Novoselov, Science **323**, 610 (2009)
15. H. Şahin, C. Ataca, S. Ciraci, Phys. Rev. B **81**, 205417 (2010)
16. R.R. Nair, W. Ren, R. Jalil, I. Riaz, V.G. Kravets, L. Britnell, P. Blake, F. Schedin, A.S. Mayorov, S. Yuan, M.I. Katsnelson, H.-M. Cheng, W. Strupinski, L.G. Bulusheva, A.V. Okotrub, I.V. Grigorieva, A.N. Grigorenko, K.S. Novoselov, A.K. Geim, Small **6**, 2877 (2010)
17. H. Şahin, M. Topsakal, S. Ciraci, Phys. Rev. B **83**, 115432 (2011)
18. C. Ataca, M. Topsakal, E. Aktürk, S. Ciraci, J. Phys. Chem. C **115**, 16354 (2011)
19. C. Ataca, H. Sahin, E. Aktürk, S. Ciraci, J. Phys. Chem. C **116**, 8983 (2011)
20. P. Hohenberg, W. Kohn, Phys. Rev. **136**, B864 (1964)
21. W. Kohn, L.J. Sham, Phys. Rev. **140**, A1133 (1965)
22. M. Topsakal, S. Cahangirov, S. Ciraci, App. Phys. Lett. **96**, 091912 (2010)
23. S. Miyake, R. Kaneko, Y. Kikuya, I. Sugimoto, J. Tribol. **113**, 384 (1991)
24. P. Thomas, K. Delbe, D. Himmel, J.L. Mansot, F. Cadore, K. Guerin, M. Dubois, C. Delabarre, A. Hamwi, J. Phys. Chem. Solids **67**, 1095 (2006)
25. J.M. Martin, C. Donnet, Th. Le Mogne, Th. Epicier, Phys. Rev. B **48**, 10583 (1993)
26. T. Liang, W.G. Sawyer, S.S. Perry, S.B. Sinnott, S.R. Phillpot, Phys. Rev. B **77**, 104105 (2008)
27. S. Chen, L. Brown, M. Levendorf, W. Cai, S.-Y. Ju, J. Edgeworth, X. Li, C.W. Magnuson, A. Velamakanni, R.D. Piner, J. Kang, J. Park, R.S. Ruoff, ACS Nano **5**, 1321 (2011)
28. J.P. Perdew, K. Burke, M. Ernzerhof, Phys. Rev. Lett. **77**, 3865 (1996)
29. S. Grimme, J. Comp. Chem. **27**, 1787 (2006)
30. P.E. Blochl, Phys. Rev. B **50**, 17953 (1994)
31. G. Kresse, J. Hafner, Phys. Rev. B **47**, 558 (1993)
32. G. Kresse, J. Furthmuller, Phys. Rev. B **54**, 11169 (1996)
33. S. Cahangirov, C. Ataca, M. Topsakal, H. Şahin, S. Ciraci, Phys. Rev. Lett. **108**, 126103 (2012)
34. S. Cahangirov, S. Ciraci, V. Ongun, Özçelik. Phys. Rev. B **87**, 205428 (2013)
35. L.C. Lew, Yan Voon, E. Sandberg, R. S. Aga, A. A. Farajian. Appl. Phys. Lett. **97**, 163114 (2010)
36. M. Houssa, E. Scalise, K. Sankaran, G. Pourtois, V.V. Afanas'ev, A. Stesmans, Appl. Phys. Lett. **98**, 223107 (2011)
37. S. Cahangirov, E. Aktürk, M. Topsakal, H. Şahin, S. Ciraci, Phys. Rev. Lett. **102**, 236804 (2009)
38. M. Dienwiebel, G.S. Verhoeven, N. Pradeep, J.W.M. Frenken, Phys. Rev. Lett. **92**, 126101 (2004)
39. J.S. Choi, J.S. Kim, I.S. Byun, D.H. Lee, M.J. Lee, B.H. Park, C. Lee, D. Yoon, H. Cheong, K.H. Lee, Y.W. Son, J.Y. Park, M. Salmeron, Science **333**, 607 (2011)
40. A.E. Filippov, M. Dienwiebel, J.W.M. Frenken, J. Klafter, M. Urbakh, Phys. Rev. Lett. **100**, 046102 (2008)
41. A.S. de Wijn, C. Fusco, A. Fasolino, Phys. Rev. E **81**, 046105 (2010)
42. I.V. Lebedeva, A.A. Knizhnik, A.M. Popov, O.V. Ershova, Y.E. Lozovik, B.V. Potapkin, Phys. Rev. B **82**, 155460 (2010)
43. A.M. Popov, I.V. Lebedeva, A.A. Knizhnik, Y.E. Lozovik, B.V. Potapkin, Phys. Rev. B **84**, 045404 (2011)
44. H. Lee, N. Lee, Y. Seo, J. Eom, S.W. Lee, Nanotechnology **20**, 325701 (2009)
45. T. Filleter, J.L. McChesney, A. Bostwick, E. Rotenberg, K.V. Emtsev, Th. Seyller, K. Horn, R. Bennewitz, Phys. Rev. Lett. **102**, 086102 (2009)
46. C. Lee, Q. Li, W. Kalb, X.Z. Liu, H. Berger, R.W. Carpick, J. Hone, Science **328**, 76 (2010)
47. A. Erdemir, Surf. Coat. Technol. **146**, 292 (2001)
48. D. Berman, A. Erdemir, A.V. Sumant, Carbon **54**, 454 (2013)
49. D. Berman, A. Erdemir, A.V. Sumant, Carbon **59**, 167 (2013)